Supporting Information

Dynamic hydrogen bubbling templated AgSn@SnO_x electrocatalyst for selective electrochemical CO_2 reduction: Adjusting the binding energy of the $HCOO^*$ intermediate

Hisham G. Elaqapa[a], Ibrahim M. Badawy[a], Ghada E. Khedr[a,b], Ahmed M. Agour[a], Doha M. Sayed[a,c], Manar M. Taha[a], Nageh K. Allam[a]*.

[a]Energy Materials Laboratory (EML), School of Sciences and Engineering, The American University in Cairo, New Cairo 11835, Egypt.

[b]Department of Analysis and Evaluation, Egyptian Petroleum Research Institute, Cairo, 11727, Egypt.

[C]Department of Chemistry, Faculty of Science, Cairo University, Cairo 12613, Egypt.

* Corresponding Author's email: nageh.allam@aucegypt.edu

1. Experimental

1.1 Materials

Copper foil (0.25 mm thickness; Alfa Aesar), $SnCl_4.xH_2O$ (Alfa Aesar, (≥99.0%)), $AgNO_3$ (Sigma Aldrich, (≥99.0%)), H_2SO_4 (Sigma Aldrich, (≥99.0%)). All high grade without further Purification. Milli-Q ultrapure water was used throughout the preparation of all solutions.

1.2 Synthesis of $AgSn@SnO_x$

Dynamic hydrogen bubbling templated electrodeposition was involved as a simple and efficient strategy to synthesize a porous foam dendritic structure of Sn metal from an electroplating solution of 0.15 M of $SnCl_4.xH_2O$ dissolved in 1.5 M H_2SO_4 on a copper sheet. First, a copper sheet was mechanically polished by a sandpaper, then soaked in a 3 M HCl solution for 5 minutes to remove any native oxide layer. Subsequently, the copper sheet was rinsed in deionized water and ethanol, in order, for five minutes under sonication to remove any traces of HCl. Then, the pre-cleaned copper mesh was masked with polytetrafluoroethylene (PTFE) tape to fix the exposed geometric surface area of the copper sheet to 1 cm^2. Afterwards, a three-electrode electrochemical setup was engaged for the galvanostatic deposition process using a counter electrode of graphite rod and $HgSO_4$ reference electrode. The galvanostatic deposition was optimized to last for 1 minute under a potential of -2.25 V that was equivalent a current density of 400-450 $mA.cm^{-2}$ with a 1 cm^2 defined distance between both the copper sheet and the counter electrode. Finally, the deposited film is dipped into 5 mM solution of $AgNO_3$ to implement the galvanic displacement, applying different periods of time (15, 30, 45 s).

1.3 Electrochemical measurements

The electrocatalytic assessments for CO_2 reduction were conducted using an H-cell design inspired by Dr. Kuhl. The H-cell comprises two acrylic plates, each with a working area of 8x8mm for placing the anode and cathode materials. A Nafion 117 membrane is placed between the two plates, and a reference electrode is inserted through a hole in the cathode compartment. CO_2 gas with a purity of 99.999% is introduced into the H-cell from the bottom at a controlled flow rate of 15 standard cubic centimeter per minute (sccm) using a mass flow controller (MFC). The product gas is directed towards the inlet valve of the gas chromatography (GC), where it is analyzed at set intervals of 13 minutes, 32 minutes, and 55 minutes with a total runtime of 60

minutes for each run. A Biologic SP300 type potentiostat/galvanostat was used for all electrochemical experiments with a 3-electrode set-up in the acrylic cell. The three electrode-system involved a counter electrode of platinized titanium mesh, and Ag/AgCl (KCl sat.) as a reference electrode. All potential values were converted to the reversible hydrogen electrode (RHE) scale by the given formula: $E_{RHE} = E_{Ag/AgCl} + 0.210\ V + 0.059\ pH$. The iR drop was compensated using 85% of the measured R_u. All current densities were normalized to the geometric area of the working electrode (1 cm^2). The protocol employed for measuring CO_2RR performance involves several steps:

- 85% iR compensation is applied, followed by a 30-minute period of open circuit potential (OCP).
- Prior to electrolysis, the electrolyte in each compartment is purged with CO_2 gas for 30 minutes.
- Chronoamperometric measurements are then taken at various operating potentials and the gaseous products are measured every 15 minutes over a one-hour period of electrolysis. The liquid product is vialed and measured after the experiment.

1.4 Product analysis

Gas phase products were measured using a gas chromatography (SRI 8610C Multi-gas #5, 6' Haysep D and 6' Molecular Sieve 5A) during the experiments. The gas chromatography was fitted with a thermal couple detector (TCD) and a flame ionization detector (FID), with Argon (99.9999%) used as the carrier gas. The system comprised of gas-lines that were directly connected to the acrylic cell and led out to the gas chromatography. The high performance liquid chromatography (HPLC) method using Eclipse XBD-C18 and acidified deionized water as the mobile phase with a flow rate of 0.6 mL/min was utilized to measure the liquid phase products. The calculation of the FE of gaseous and liquid products was done by the following equation:

$$FE = \frac{zFn}{it} \qquad (1)$$

Where (z) is the number of electrons transferred to produce one mole of product (i.e., z = 2 for all products generated in this work), (F) is the faraday constant of 96485 $C.mol^{-1}$, (n) is the number

of moles of products; quantified by GC and HPLC, (I) is the current density in Ampere (A), and (t) is the reaction time in seconds.

2. Materials characterization

Powder XRD analysis was implemented via a D8 Discover(Bruker). The samples morphology were investigated by scanning electron microscope (SEM, Model JSM-760F). Energy-dispersive X-ray spectrometer (EDS) mapping was conducted using JEM-ARM 200F. TEM imaging and selected area electron diffraction (SAED) studies were carried out using Talos-F200i TEM. The elemental composition of the surface and the valence states of the samples were analyzed through X-ray photoelectron spectroscopy (XPS) with Al Kα radiation.

3. Computational details

Binding energies of the intermediates on SnO (101) and AgSn@SnO were calculated using Vienna Ab initio Simulation Package (VASP) software with Vanderbilt ultrasoft pseudopotentials. A supercell of 3×3×3 was created from SnO and AgSn. (101) surface was cleaved from SnO supercell; the core shell system was designed using VESTA. To prevent interactions with periodic images, a vacuum slab with a thickness of 15 Å was constructed. The calculations employed the generalized gradient approximation (GGA) with the Perdew−Burke−Ernzerhof (PBE) functional. The cut-off energy was set to 500 eV, and a self-consistent field (SCF) tolerance of 1.0×10^{-8} eV was used. The Brillouin zone was sampled using a Monkhorst−Pack k-point grid of 3×3×1. For relaxation, we used conjugate gradient (CG) algorithm. VASPsol software was used to investigate the water-solvent effect on all the intermediates. It is an implicit solvation model which is based on Polarizable Continuum Model (PCM).

The optimization of the free CO_2 molecule was performed within a 10×10×10 Å unit cell. The resulting optimized C-O bond length and O-C-O angle were found to be 1.178 Å and 180.0°, respectively, which align with available experimental and theoretical data. The adsorption energy of CO_2 is calculated using the following equation:

$E_{ads} = E_{CO2}$+surface - (E_{CO2} + $E_{surface}$)

Here, E_{CO2}+surface represents the energy of the surface with the adsorbed CO_2, E_{CO2} represents the energy of the free CO_2 molecule, and $E_{surface}$ represents the energy of the surface. The Cu site was selected for adsorption. The adsorption energies were calculated relative to H_2(g) as:

$$\Delta E = E_{slab+H} - E_{slab} - \tfrac{1}{2}E_{H2}$$

The associated free energy of H is given by:

$$\Delta G = \Delta E + \Delta ZPE - T\Delta S$$

Here, ΔZPE represents the difference in zero-point energy, and ΔS represents the difference in entropy between the adsorbed state and the gas phase. Considering that ΔZPE - TΔS is approximately 0.24 eV, we can calculate ΔG as ΔE + 0.24 eV.

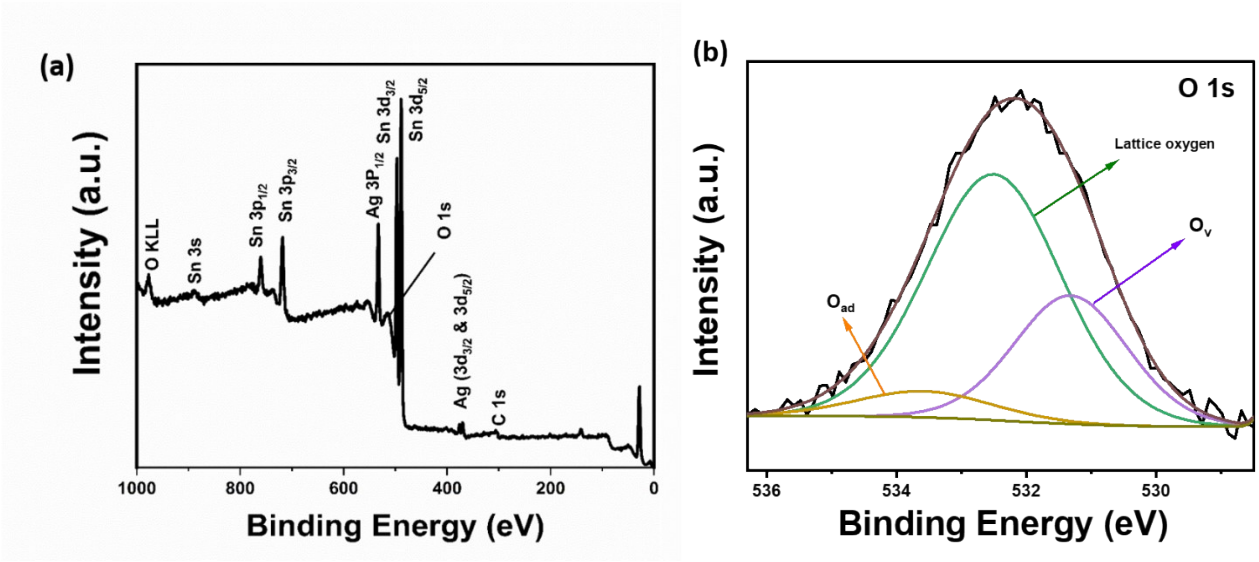

Figure S1. (a) Spectrum survey, (b) O1s spectrum of AgSn@SnO_x(30 sec).

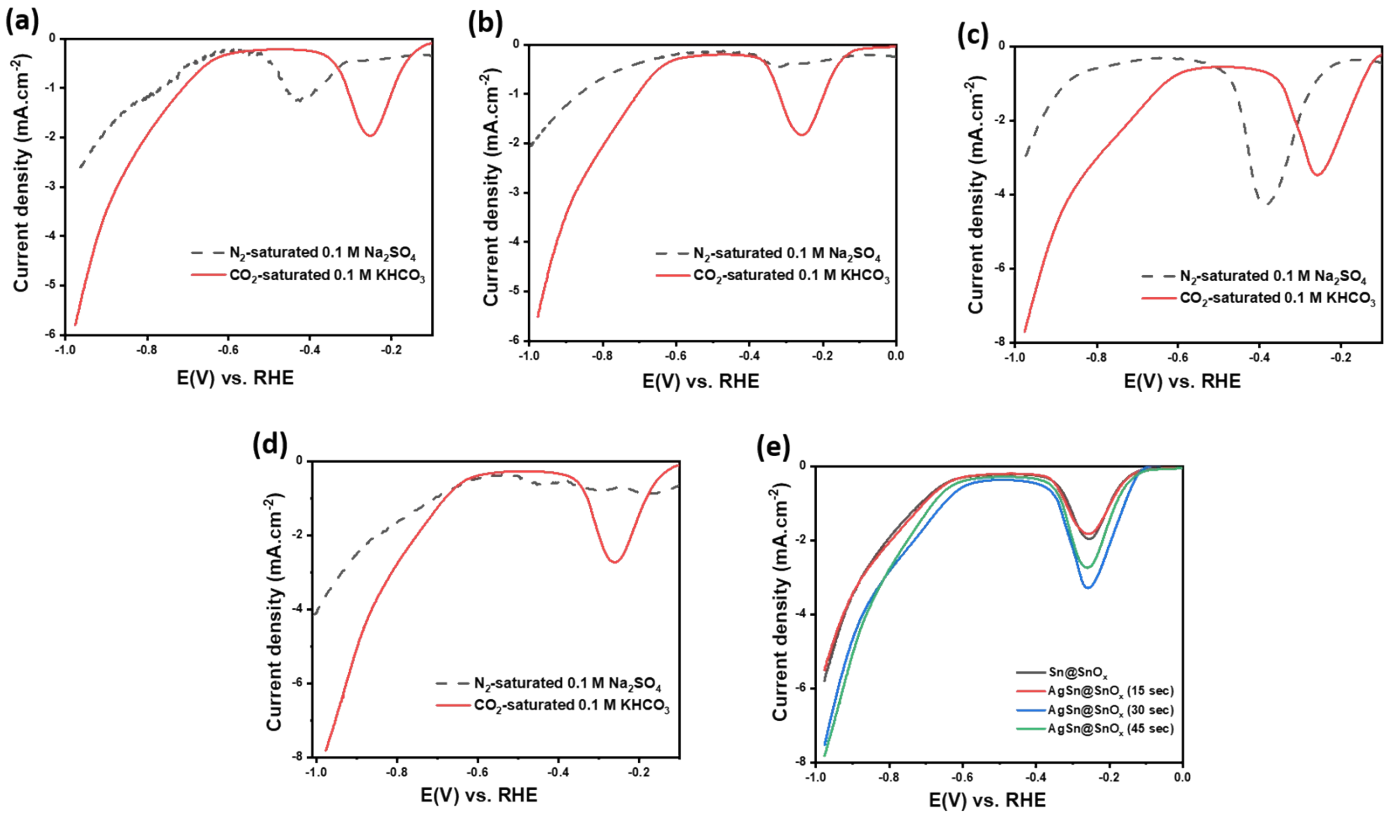

Figure S2. Polarization curves of (a) Sn@SnO_x, (b) AgSn@SnO_x (15 s), (c) AgSn@SnO_x(30 s), and (d) AgSn@SnO_x(45 s) in N_2-satuatred 0.1 M Na_2SO_4, and CO_2-satuarated 0.1 M $KHCO_3$. Scan rate=10 $mV.s^{-1}$(e) LSV profiles of the different catalysts in CO_2-satuarated 0.1 M $KHCO_3$. Scan rate=10 $mV.s^{-1}$

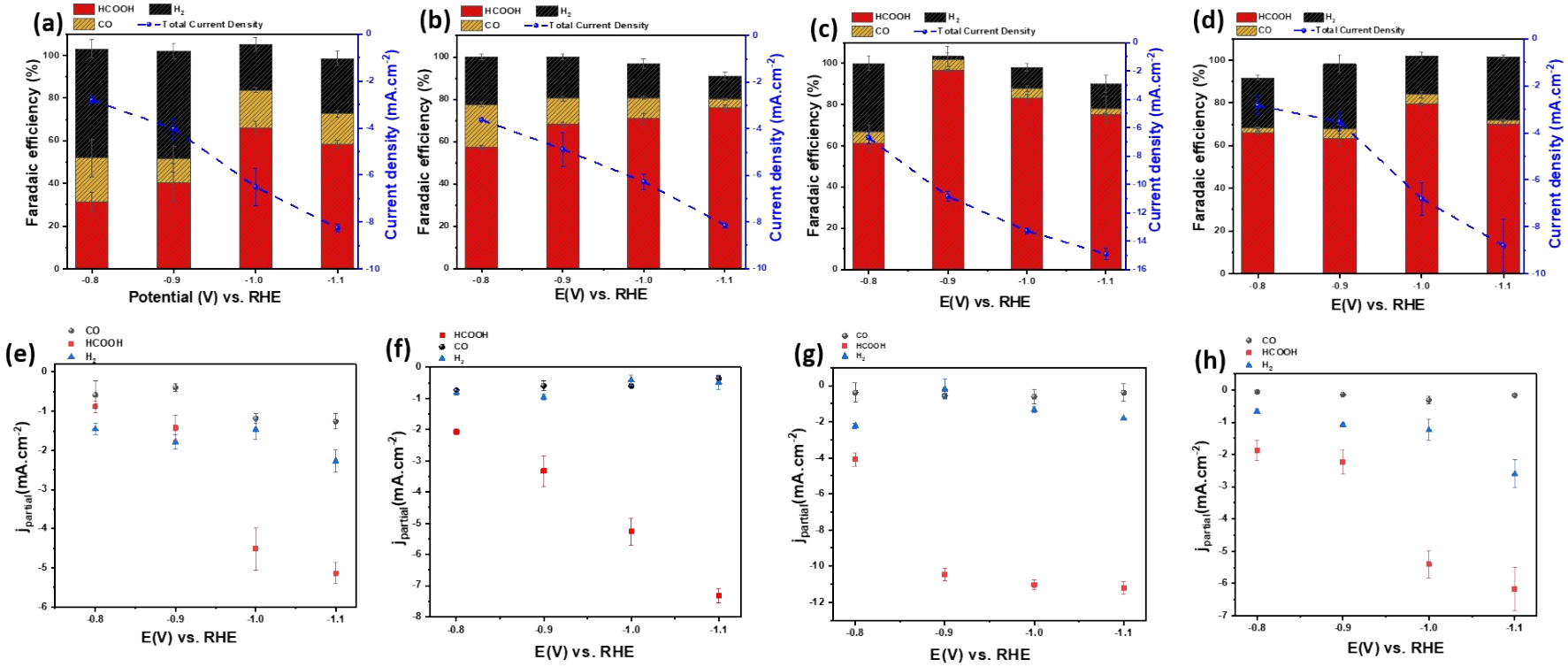

Figure S3. Total current densities, faradaic efficiencies of CO, H_2, and HCOOH, and their corresponding partial current densities at different potentials vs. RHE; (a-e) Sn@SnO_x, (b-f) AgSn@SnO_x(15 s), (c-g) AgSn@SnO_x(30 s), (d-h) AgSn@SnO_x(45 s). Error bars represent the standard deviation, obtained by studying three different electrodes.

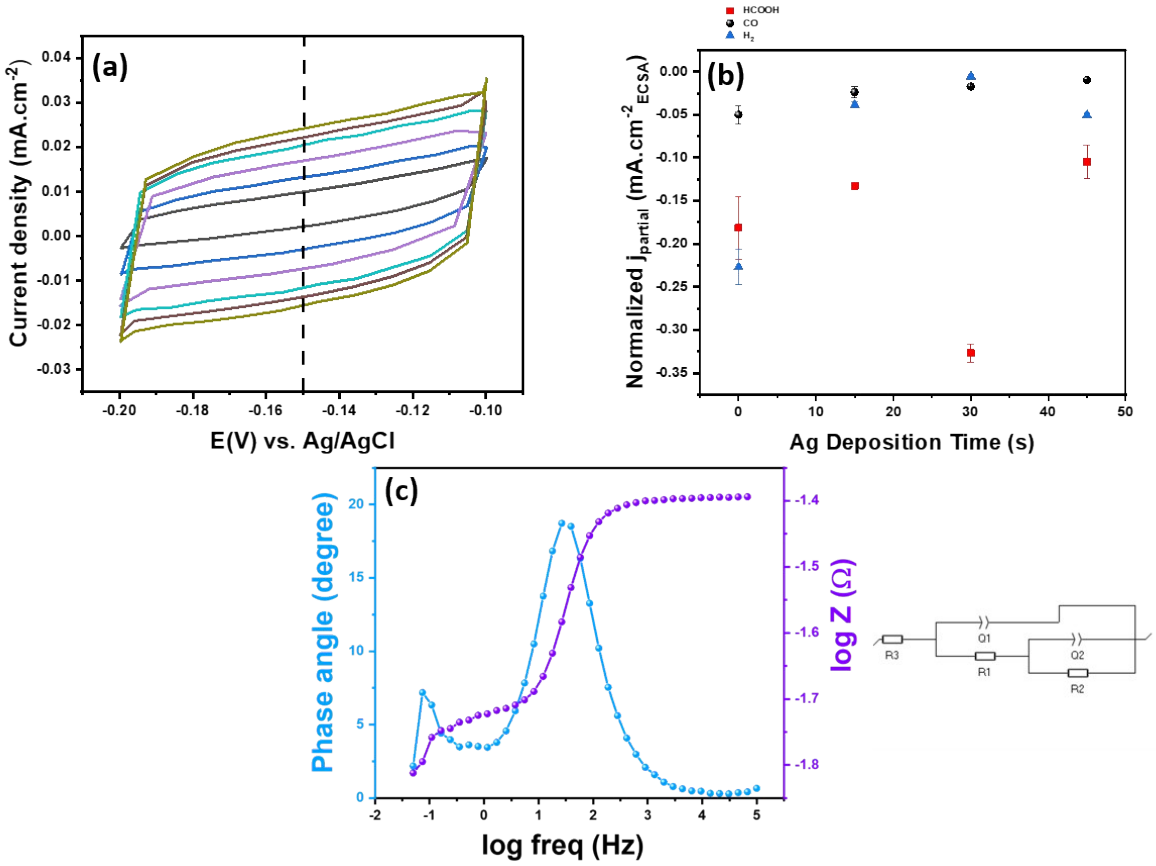

Figure S4. (a) CVs at the non-faradaic region between -0.1 and -0.2 V vs. Ag/AgCl (KCl sat.) for AgSn@SnO_x(30 s) in 0.1 M CO_2-saturated $KHCO_3$. (b) Normalized partial current densities corresponding to HCOOH, CO, H_2 for AgSn@SnO_x(30 s). (c) Potentioelectrochemical impedance spectroscopy in the Bode plot format and equivalent circuit.

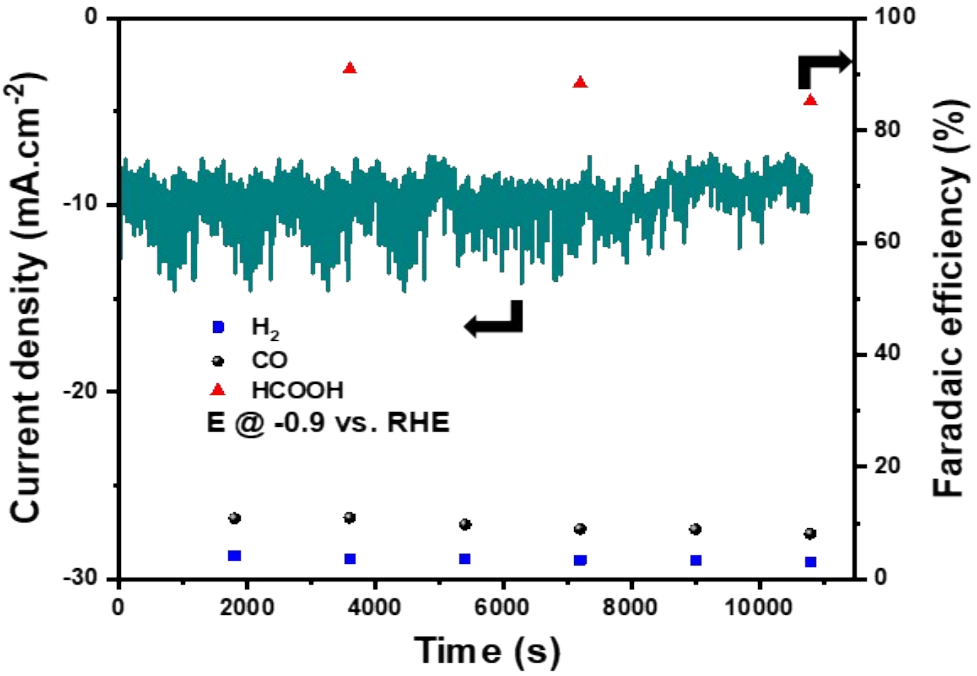

Figure S5. Chronoamperometry run and faradaic efficiencies of HCOOH, CO, H_2 demonstrates the stabilty of AgSn@SnO_x (30 s) over 3 hours at -0.9 V vs. RHE.

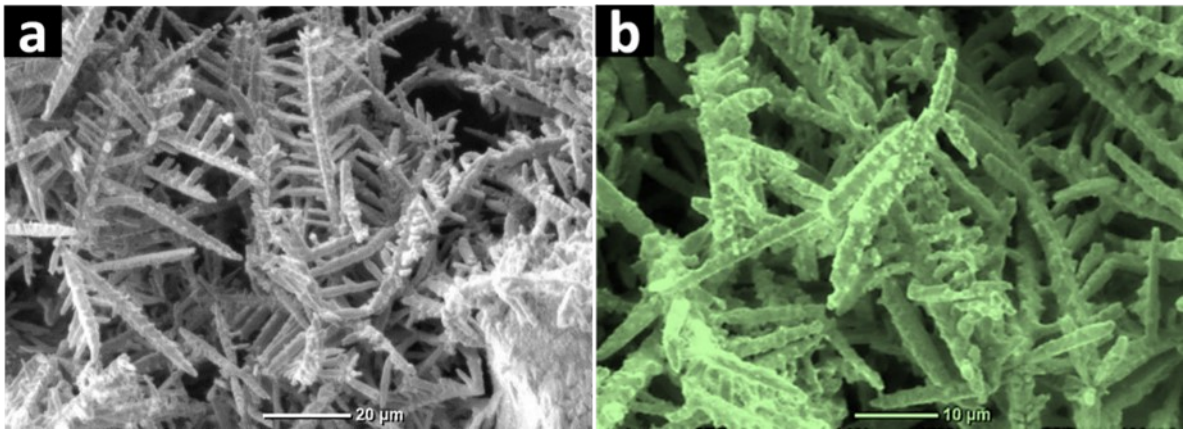

Figure S6. SEM images of AgSn@SnO_x(30 s) (a) before, (b) after 1 hour of CO_2 electrolysis.

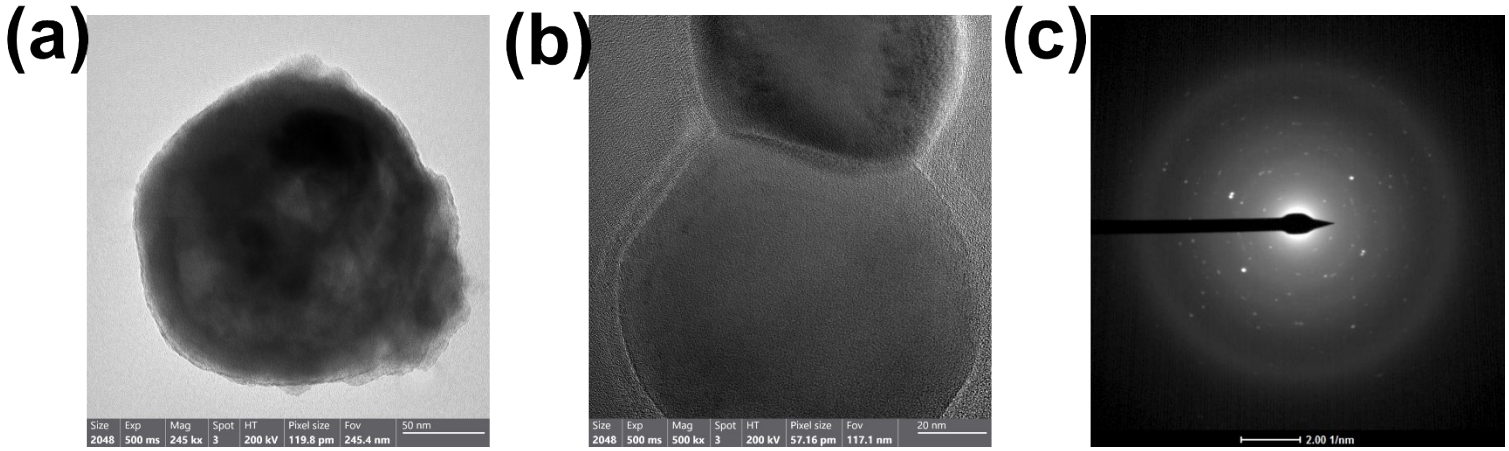

Figure S7. HRTEM (a)SnAg@SnO_x(30 s), (b) Sn@SnO_x, (c) SAED pattern of Sn@SnO_x.

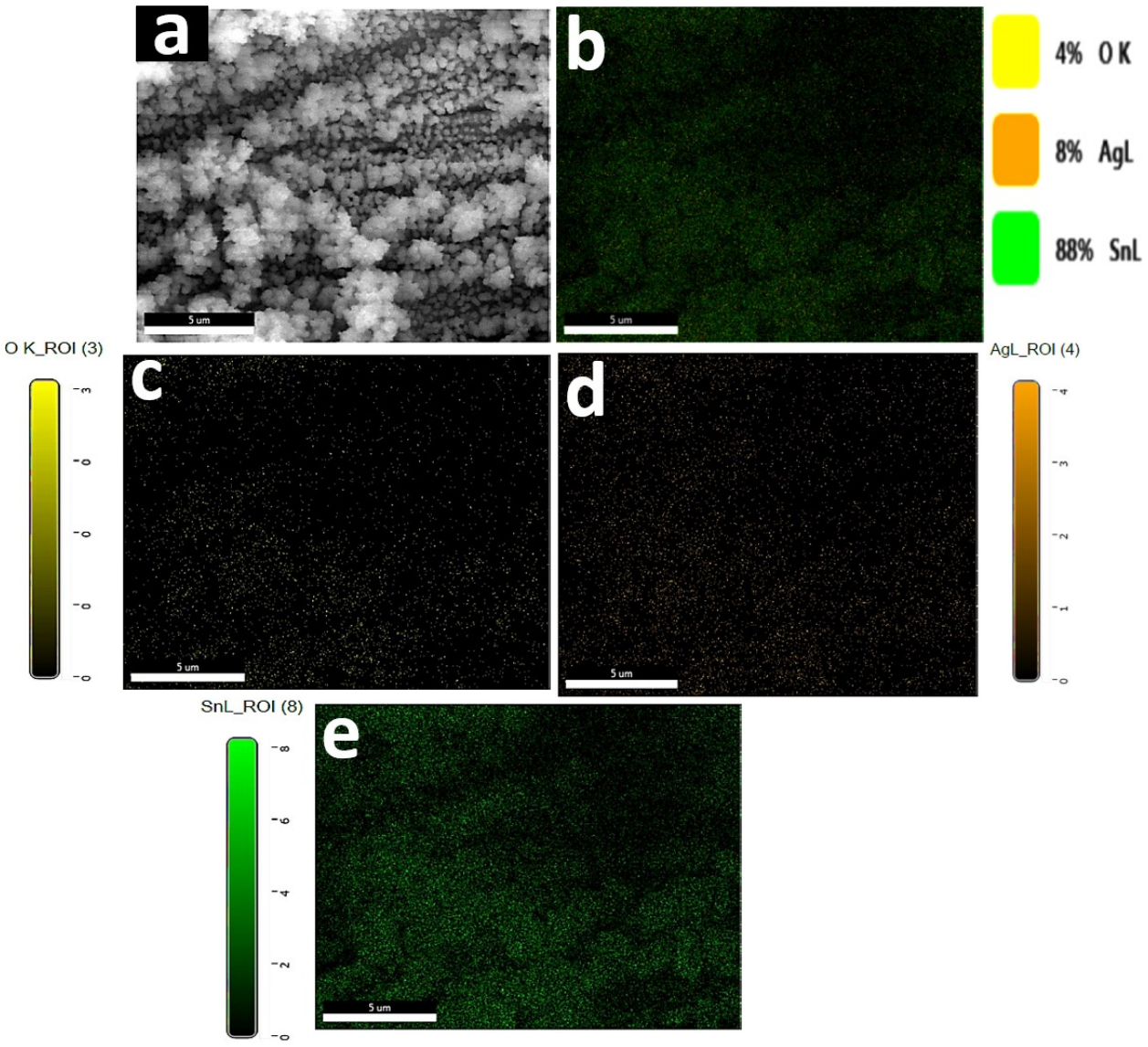

Figure S8. EDX mapping of AgSn@SnO_x(30 s). (a) AgSn@SnO_x(30 s) selected region for mapping, (b) elements distribution in the sample, (c) Oxygen, (d) Silver, (e) Tin.

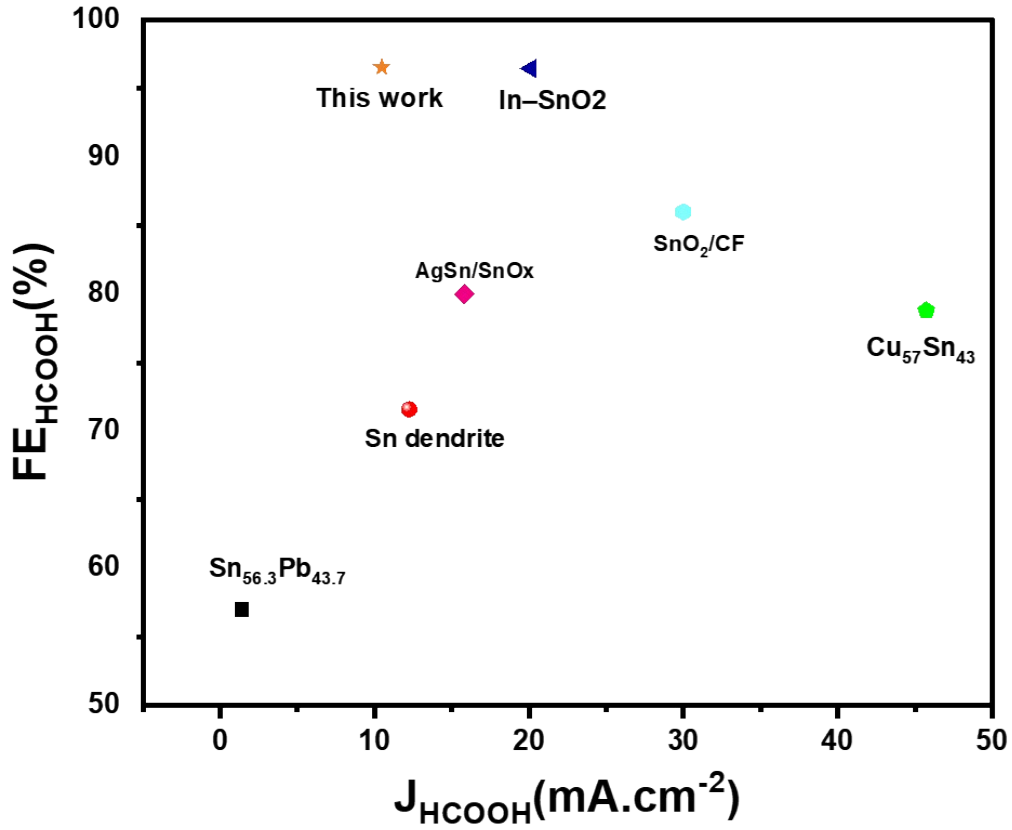

Figure S9. Comparison between the electrocatalytic performance of different Sn-based catalysts.

Table S1. Extracted data from non-faradaic cyclic voltammetry measurements for the different catalysts.

Catalyst	C_{dl} (μF.cm^{-2})	ECSA	Roughness	R^2
Sn@SnO$_x$	359.34	8.98	7.33	0.99380
AgSn@SnO$_x$ (15 sec)	1000.35	25	20.41	0.99944
AgSn@SnO$_x$ (30 sec)	1280.41	32.01	26.13	0.99764
AgSn@SnO$_x$ (45 sec)	858.12	21.45	17.51	0.99885

In order to determine the electrochemically active surface area (ECSA) of the electrodes, a technique involving the measurement of double-layer capacitance (Cdl) was employed. This was done by taking cyclic voltammograms in a non-faradaic region with a potential range between --0.1 and -0.2 V vs. Ag/AgCl (KCl sat.), at varying scan rates of 20, 40, 60, 70, 90, and 100 mV s-1. The differences in anodic and cathodic current densities (Δj or ja-jc) at -0.15 V were plotted against the scan rates, and a linear regression was performed on the resulting data. The slope of the line generated from the regression analysis gives the double-layer capacitance (Cdl), which is proportional to the electrochemically active surface area (ECSA) of the electrodes:

$$ECSA = Cdl/40 \quad (2)$$

where the value of 40 is the capacitance of a flat surface. The roughness factor of the catalysts was estimated by the given equation:

$$RF = Cdl(catalyst)/Cdl(substrate) \quad (3)$$

Table S2. Electrocatalytic activity of different catalysts at different operating potentials.

Applied potential (V vs. RHE)	Number of experiments	Total current densities (mA.cm^{-2})	FE % (H_2)	FE % (CO)	FE % (HCOOH)
Electrocatalytic performance of Sn@SnO_x.					
-0.8	3	-2.81 ± 0.15835	51.0902 ± 4.23783	20.6848 ± 8.79514	31.225 ± 4.5573
-0.9	3	-4.032 ± 0.43962	50.52962 ± 3.4073	11.1233 ± 6.15895	40.41 ± 8.90323
-1	3	-6.51 ± 0.79074	21.48723 ± 3.11092	17.45278 ± 1.16956	66.24 ± 2.91855
-1.1	3	-8.26 ± 0.17051	25.84145 ± 3.26701	14.33778 ± 1.62299	58.375 ± 1.64402
Electrocatalytic performance of AgSn@SnO_x(15 sec).					
-0.8	3	-3.62 ± 0.07657	22.51973 ± 1.50709	20.3636 ± 1.331	57.11667 ± 1.01231
-0.9	3	-4.88 ± 0.72121	19.7282 ± 1.25607	12.2018 ± 0.98449	68.07 ± 1.01157
-1	3	-6.28 ± 0.33689	16.3163 ± 2.25199	9.8737 ± 0.81999	70.81 ± 2.51731
-1.1	3	-8.15 ± 0.09731	10.90813 ± 1.8502	4.29187 ± 0.59135	75.8 ± 1.628
Electrocatalytic performance of AgSn@SnO_x(30 sec).					
-0.8	3	-6.70 ± 0.42865	33.26 ± 3.60792	5.72 ± 3.5075	61 ± 3.46255
-0.9	3	-10.84 ± 0.34635	1.65 ± 4.87806	5.10 ± 3.30623	96.55 ± 0.67334
-1	3	-13.26 ± 0.22358	10.07 ± 2.02279	4.59 ± 1.35698	83.23 ± 1.83093
-1.1	3	-14.90 ± 0.42412	12.17 ± 4.14993	2.59 ± 6.35987	75.23 ± 0.44258
Electrocatalytic performance of AgSn@SnO_x(45 sec).					
-0.8	3	-2.84 ± 0.38459	23.42 ± 1.10912	2.22 ± 0.25553	66.08 ± 0.91871
-0.9	3	-3.53 ± 0.40005	30.69 ± 3.90858	4.20 ± 1.8893	63.46 ± 3.42605
-1	3	-6.81 ± 0.69133	18.24 ± 1.52847	4.66 ± 1.58795	79.35 ± 0.67192
-1.1	3	-8.8 ± 1.10145	29.56 ± 0.89354	1.97 ± 0.23608	70.09 ± 1.11719

Table S3. Comparison the catalytic activity of AgSn@SnO_x with the literature.

Catalyst	Operating Potential (V vs. RHE)	Total Current Density (mA.cm^{-2})	Partial Current Density (mA.cm^{-2})	Faradaic Efficiency (FE $_{HCOOH}$ %)	Ref.
AgSn@SnO_x (30 sec)	-0.9	10.84	10.46	96 %	This work
$Sn_{56.3}Pb_{43.7}$	-1.36	57.3	45.73	78.8 %	[1]
$Cu_{57}Sn_{43}$	-0.92	2.5	1.42	57 %	[2]
Sn/SnO_x	-0.7	1.8	1.04	58 %	[3]
AgSn/SnO_x	-0.8	19.7	15.8	80 %	[4]
SnO_2 /graphene	-1.16	10.2	9.55	93.6 %	[5]
Sn dendrite	-1.36	17.1	12.24	71.6 %	[6]
Sn-graphene	-1.16	21.1	18.78	89 %	[7]
Cu@Sn	-0.93	-	16.52	100 %	[8]
SnO_2/CF	-1	-	30	86%	[9]
In–SnO_2	-0.75	-	20.12	96.46%	[10]

References

[1] S. Y. Choi, S. K. Jeong, H. J. Kim, I.-H. Baek, and K. T. Park, 'Electrochemical Reduction of Carbon Dioxide to Formate on Tin–Lead Alloys', ACS Sustain Chem Eng, vol. 4, no. 3, pp. 1311–1318, Mar. 2016, doi: 10.1021/acssuschemeng.5b01336.

[2] M. Watanabe, M. Shibata, A. Kato, M. Azuma, and T. Sakata, 'Design of Alloy Electrocatalysts for CO_2 Reduction: III . The Selective and Reversible Reduction of CO_2 on Cu Alloy Electrodes', J Electrochem Soc, vol. 138, no. 11, p. 3382, Nov. 1991, doi: 10.1149/1.2085417.

[3] Y. Chen and M. W. Kanan, 'Tin Oxide Dependence of the CO_2 Reduction Efficiency on Tin Electrodes and Enhanced Activity for Tin/Tin Oxide Thin-Film Catalysts', J Am Chem Soc, vol. 134, no. 4, pp. 1986–1989, Feb. 2012, doi: 10.1021/ja2108799.

[4] W. Luc et al., 'Ag-sn bimetallic catalyst with a core-shell structure for CO_2 reduction', J Am Chem Soc, vol. 139, no. 5, pp. 1885–1893, Feb. 2017, doi: 10.1021/jacs.6b10435.

[5] S. Zhang, P. Kang, and T. J. Meyer, 'Nanostructured Tin Catalysts for Selective Electrochemical Reduction of Carbon Dioxide to Formate', J Am Chem Soc, vol. 136, no. 5, pp. 1734–1737, Feb. 2014, doi: 10.1021/ja4113885.

[6] D. H. Won, C. H. Choi, J. Chung, M. W. Chung, E.-H. Kim, and S. I. Woo, 'Rational Design of a Hierarchical Tin Dendrite Electrode for Efficient Electrochemical Reduction of CO_2', ChemSusChem, vol. 8, no. 18, pp. 3092–3098, 2015, doi: https://doi.org/10.1002/cssc.201500694.

[7] F. Lei et al., 'Metallic tin quantum sheets confined in graphene toward high-efficiency carbon dioxide electroreduction', Nat Commun, vol. 7, no. 1, p. 12697, 2016, doi: 10.1038/ncomms12697.

[8] X. Hou et al., '3D core–shell porous-structured Cu@Sn hybrid electrodes with unprecedented selective CO_2-into-formate electroreduction achieving 100%', J. Mater. Chem. A, vol. 7, no. 7, pp. 3197–3205, 2019, doi: 10.1039/C8TA10650A.

[9] H. Li et al., 'Promoting the electroreduction of CO_2 with oxygen vacancies on a plasma-activated SnO_x/carbon foam monolithic electrode', J. Mater. Chem. A, vol. 8, no. 4, pp. 1779–1786, 2020, doi: 10.1039/C9TA12401B.

[10] X. Zhao et al., 'Enhanced electron transfer by In doping in SnO_2 for efficient CO_2 electroreduction to C_1 products', Chem. Commun., vol. 58, no. 91, pp. 12716–12719, 2022, doi: 10.1039/D2CC05042K.